Submitted to *Solar Energy Materials and Solar Cells*
Special Issue: Advances in thermophotovoltaics: materials, devices and systems
Revised Nov. 3rd

Improved performance of a near-field thermophotovoltaic device by a back gapped reflector

Dudong Feng, Shannon K. Yee, and Zhuomin M. Zhang*
The George W. Woodruff School of Mechanical Engineering
Georgia Institute of Technology, Atlanta, GA 30332, USA

*Corresponding Author: zhuomin.zhang@me.gatech.edu

ABSTRACT

Various spectral control techniques can be applied to improve the performance of a thermophotovoltaic (TPV) device. For example, a back surface reflector (BSR) is a common structure to improve the performance of TPV devices. A conventional metal BSR structure enhances the photogeneration rate by increasing the absorption probability of photons via back surface reflections, affording a second chance for absorption. However, the effects of surface passivation and external luminescence introduced by BSR structures have been previously ignored, which potentially decreases the performance of TPV devices. Recently, a back gapped reflector (BGR) structure was proposed to greatly improve the performance of far-field TPV devices by reducing imperfect reflections at the semiconductor-metal interface. In the present work, the performance improvement on a thin-film, near-field InAs TPV device with a BGR is investigated, comparing its performance to that with a conventional metal BSR. Surface passivation conditions are also investigated to further improve the performance of TPV devices with back reflectors. The output power and efficiency are calculated using an iterative model combining fluctuational electrodynamics and the full drift-diffusion model. For the well-passivated condition, when the BSR is replaced by the BGR, the calculated conversion efficiency of the near-field TPV was improved from 16.4% to 21% and the output power was increased by 10%. Finally, the absorption of the back reflectors and external luminescence loss are analyzed to explain the performance improvement.

Keywords: back gapped reflector; back surface reflector; near-field thermophotovoltaics; external luminescence; surface recombination and passivation; performance improvement.

1. Introduction

Thermophotovoltaics (TPVs) convert thermal radiation into electricity from terrestrial heat sources. A TPV device consists of three main components: an emitter that radiates photons by consuming thermal energy from a heat source, a TPV cell that converts incident photons into electricity, and a vacuum gap between the emitter and cell. With the benefits of compact size and solid-state operation, TPV devices could achieve widespread applications enabling local thermal energy storage [1, 2], waste heat recovery [3, 4], aerospace power generation [5, 6], nuclear power conversion [7, 8], and direct solar energy conversion [9-16]. Among various applications, solar thermophotovoltaics (STPVs) is a promising electricity generating technology that possesses a high theoretical system efficiency of 54% without using concentration or a selective absorber [17], and exceeds the Shockley-Queisser limit of 33.7%. Datas and Algora [16] developed a practical STPV device using HfO_2 coated tungsten as the absorber and emitter, which exhibited 0.8% system efficiency. Lenert *et al*. [10] experimentally demonstrated a multiwalled carbon nanotube STPV device with 3.2% efficiency. Bierman *et al*. [15] further improved the solar-to-electrical efficiency reaching 6.8% with a one-dimensional photonic crystal selective emitter and a tandem plasma-interference optical filter. Recently, Bhatt *et al.* realized a STPV system with the overall conversion efficiency of 8.4% by using a nanostructure-based selective emitter [18]. The primary difference between the practical efficiency and theoretical efficiency of STPVs suggests that even greater performance can be achieved.

Current efforts have been directed toward optimizing the photon emission and absorption processes to match the bandgap energy of cell materials, which is the primary approach to realizing high efficiency TPV devices [17, 19, 20]. Several research groups have achieved wavelength selectivity and direction-insensitivity on TPV emitters using periodic nanostructures including gratings [21-24], nanowires [25], and photonic crystals [26], which also exhibit enhanced emittance by the excitations of surface polaritons and cavity resonance. Considering the working temperature of TPV systems (*e.g.*, 600-1300 K), narrow bandgap semiconductor materials are preferred to produce larger output power density than regular solar cell materials [4, 14, 27].

Additionally, near-field radiation has been proposed as one of the promising mechanisms to greatly enhance the performance of TPV devices by Whale and Carvalho [28]. When the vacuum gap distance is reduced to the microscale or even nanoscale, additional coupled evanescent photons tunnel through the gap and dominate the radiation exchange between the emitter and cell [29]. Significant experimental progress has been made in recent years [29-35]. To further optimize the efficiency and boost the output power density of near-field TPV devices, the similar spectral control techniques mentioned above can also be applied [36-39].

A back reflector is a common way to improve the performance of a TPV device by increasing the interband absorption while recycling photons below the bandgap energy [40, 41]. Two different BSRs were investigated for a far-field Ge TPV cell by Fernandez *et al*. [42]. The proposed dielectric BSR can feature high infrared reflection and excellent surface passivation of the backside of Ge TPV cells; however, the effect of the absorption of BSRs on the TPV performance has not been discussed. A parametric study on the effects of a BSR and surface recombination on a near-field InGaSb TPV device was performed by Bright *et al.* [41]. This parametric study used a combined model that neglected the near-field effects on the dark current and internal luminescence, which might be important for certain TPV devices [43, 44]. Recently, Fan *et al.* [45] proposed a thin-film TPV cell design with a BGR, which can greatly enhance the performance of a far-field InGaAs TPV device by reducing the absorption in the back reflector. Inoue *et al*. investigated the performance improvement of non-contact reflectors on both sides of a Si-based TPV device [46]. Similar structures have not been applied to near-field thin-film TPV devices, which may see even greater improvements in device performance.

In this paper, a thin-film InAs TPV device with a BGR is investigated using a newly proposed photon-charge coupled iterative model [44]. By comparing to a conventional metal BSR with different surface passivation conditions, the performance enhancement potential of this BGR is investigated for both far- and near-field regimes. The radiation exchange carried by propagating waves and evanescent waves are separately discussed for different vacuum spacings. The back gap thickness of the BGR is varied to optimize the efficiency of the InAs TPV device. The efficiency reduction, due to imperfect reflections at the semiconductor-metal interface, and output power loss, due to external luminescence and surface recombination, are also analyzed. Note, the loss

mechanisms also depend on the back gap thickness of the BGR, which can potentially guide the design and optimization of TPV devices with higher efficiency and larger output power.

2. Methodology

A thin-film InAs TPV device with a BGR (TPV-BGR) is shown in Fig. 1a, which is compared with a TPV device with a conventional BSR (TPV-BSR) shown in Fig. 1b. A vacuum gap with a variable thickness (d) separates the tungsten emitter and InAs TPV cell. The tungsten emitter is modeled as an infinitely thick bulk with temperature at T_e = 900 K. The p-doped and n-doped InAs layers with thicknesses of $d_p = d_n$ = 200 nm, are respectively subdivided by a 50-layer nonuniform mesh to consider the localization effect on photogeneration and photon chemical potential [44]. Au is used for both BGR and BSR, and the thickness d_{Au} is chosen to be 100 nm to ensure all incident photons are reflected or absorbed. The front metal grid and the back metal grid are ignored in the radiation exchange due to the low shading area (less than 5%). The back metal grid in the BGR structure is used to support the vacuum gap between the cell and the back reflector. Consequently, the series resistance of the grid and the busbar is ignored in the charge transport model. The temperature of the InAs cell (including BSR or BGR) is assumed to be room temperature, T_c = 300 K. Both devices require a vacuum environment to minimize the convection between the emitter and cell.

The charge transport equations for each layer are prescribed by full drift-diffusion model expressed as [44]:

$$\nabla \cdot \left(\varepsilon_r \nabla \varphi \right) = \left(q / \varepsilon_0 \right) \left(N_A - N_D + n - p \right) \tag{1}$$

$$\frac{\partial n}{\partial t} = \frac{1}{q} \nabla \cdot J_e + g - r_{Auger} - r_{SRH} \tag{2}$$

$$\frac{\partial p}{\partial t} = -\frac{1}{q} \nabla \cdot J_h + g - r_{Auger} - r_{SRH} \tag{3}$$

where ε_r is the dielectric constant of the cell material, and ε_0 is the vacuum permittivity. φ is the electrostatic potential, and q is the elementary charge. N_A and N_D are the acceptor and donor concentrations, respectively. Note that n and p are the electron and hole concentrations, which are functions of time (t) and space. This transient model is used to solve the steady-state condition of a TPV cell and detailed procedures can be found in Ref. [43].

The net photogeneration rate per unit volume is uniformly distributed inside layer *j*, which is solved by fluctuational electrodynamics with 100% internal quantum efficiency:

$$g = \sum_{m \neq j} \int_{\omega_g}^{\infty} \left[\Psi\left(\omega, T_m, \mu_m\right) - \Psi\left(\omega, T_j, \mu_j\right) \right] \Upsilon_{mj}\left(\omega\right) \frac{d\omega}{\Delta z_j} \tag{4}$$

where ω is the angular frequency, $\omega_g = E_g/\hbar$ is the frequency that corresponds to the bandgap energy (E_g) with $\hbar$ being the reduced Planck constant, and T and μ are the absolute temperature and photon chemical potential of the corresponding layer, respectively. Δz_j is the thickness of layer *j*. The function Ψ is the modified Bose-Einstein distribution [44]. The function Υ_{mj} is the fraction of photons emitted at a given frequency from layer *m* that is absorbed by layer *j* and vice versa. The detailed expression can be found in Ref. [44, 47]. Note, nonlocal effects of the optical response are neglected in this model [48, 49].

The Auger recombination and the Shockley-Read-Hall (SRH) recombination rate are calculated respectively as follows [44]:

$$r_{\text{Auger}} = \left(C_e n + C_h p\right)\left(np - n_i^2\right) \tag{5}$$

and

$$r_{\text{SRH}} = \frac{np - n_i^2}{\tau_p (n + n_{t,b}) + \tau_n (p + p_{t,b})} \tag{6}$$

where C_e and C_h are the Auger recombination coefficients for electrons and holes, n_i is the intrinsic carrier concentration, τ_n and τ_p are the bulk lifetimes for electrons and holes, respectively. $n_{t,b}$ and $p_{t,b}$ are the electron and hole trap concentrations that are set to be the same as the n_i in the modeling.

The charge current densities, J_e and J_h, are modeled in terms of drift and diffusion forces as follows:

$$J_e = -q\upsilon_e n \nabla\varphi + qD_e \nabla n \tag{7}$$

$$J_h = -q\upsilon_h p \nabla\varphi + qD_h \nabla p \tag{8}$$

where υ_e and υ_h are the mobility of electrons and holes, respectively, and D_e and D_h are the diffusion coefficients, which are related to mobility according to Einstein's relation $D = \upsilon k_B T / q$ for each type of carrier. The electron and hole mobilities are functions of temperature and doping concentration, which is calculated by a Caughey-Thomas-like model [44, 50]. Ohmic contact is assumed and governing equations (1), (2), and (3) are solved by applying the following boundary conditions:

$$J_{(e,h)}(z_s) = qS_{(e,h),(n,p)}\left[n(z_s) - n_0(z_s)\right] \tag{9}$$

where $S_{e,p}$, $S_{h,p}$, $S_{e,n}$, and $S_{h,n}$ are the surface recombination velocities for electrons and holes in the *p* and *n* regions, respectively, and n_0 and p_0 are the carrier concentrations at equilibrium. z_s represents the location at the top surface of *p*-InAs and bottom surface of *n*-InAs.

Equation (4) is a function of the spatial profile of photon chemical potential, which is the solution of Eqs. (1), (2), and (3). Therefore, an iterative method is required to solve this coupled transport problem. The general procedure of this iterative solver can be found in Ref. [44].

The net rate of absorbed energy of layer *j* from the tungsten emitter can be calculated by

$$Q_j = \sum_m^{emitter} \int_0^\infty \hbar\omega\left[\Psi(\omega, T_m, \mu_m) - \Psi(\omega, T_j, \mu_j)\right]\Upsilon_{mj}(\omega)d\omega \tag{10}$$

The total absorbed power for a practical TPV device should include the absorption by the back reflector, since extra work is required to remove this parasitic heating. Therefore, the conversion efficiency is calculated by

$$\eta(V) = \frac{J(V)V}{Q_{cell}}, \text{ where } Q_{cell} = \sum_j^{cell} Q_j \tag{11}$$

Here, the summation is over the InAs layers and the back reflectors. Therefore, the absorbed power of the Au layer is taken into account in calculating the efficiencies.

3. Results and Discussion

The dielectric function of tungsten at T_e is assumed to be identical to that at room temperature [51]. The dielectric function of InAs is taken from Ref. [52] considering the lattice vibration

contributions and the free-carrier contributions with a fixed doping concentration. A Drude model is used to describe the dielectric function of Au [29], $\varepsilon(\omega) = \varepsilon_\infty - \omega_p^2 / (\omega^2 + i\gamma\omega)$, where $\varepsilon_\infty = 1$, $\omega_p = 1.37 \times 10^{16}$ rad/s, and $\gamma = 5.31 \times 10^{13}$ rad/s [41]. The doping concentrations of acceptor and donor are set as $N_A = 8 \times 10^{17}$ cm^{-3} and $N_D = 2 \times 10^{16}$ cm^{-3}, respectively [44]. The difference of the InAs dielectric function caused by the different doping concentrations is neglected. The intrinsic concentration is $n_i = 6.06 \times 10^{14}$ cm^{-3} for InAs at room temperature. For Auger and SRH recombination, the following parameters are used: $C_e = C_h = 2.26 \times 10^{-27}$ cm^6 s^{-1} and $\tau_e = \tau_h = 100$ ns [53]. The values for mobilities in *p*- and *n*- regions are as follows: $\upsilon_{e,p} = 18300$ cm^{-2} V^{-1} s^{-1}, $\upsilon_{h,p} = 166$ cm^{-2} V^{-1} s^{-1}, $\upsilon_{e,n} = 26800$ cm^{-2} V^{-1} s^{-1}, and $\upsilon_{h,n} = 370$ cm^{-2} V^{-1} s^{-1} [44].

To distinguish the two vacuum gaps in the device, the vacuum spacing represents the distance between the emitter and cells; while the gap thickness refers to the distance between the cell and the back reflector. In the following, the vacuum spacing is chosen as d = 1 mm or d = 10 nm to investigate the effect of this BGR on the TPV device under either the far- or near-field regime, respectively. The gap thickness of the BGR is represented by h, which is parametrically swept between 10 nm to 10 μm. The maximum efficiency and maximum output power are calculated as a function of the gap thickness of BGR for both working regimes. Surface passivation conditions can potentially affect the performance of TPV devices [41, 42, 54, 55]. A well-passivated surface usually has large surface recombination velocity for majority carriers and small surface recombination velocity for minority carriers [56]. The surface recombination velocity for majority carriers is set to be an extremely large number, e.g., 10^9 cm/s. The surface recombination velocity for minority carriers can vary from 10^2 cm/s to 10^4 cm/s or larger depending on surface passivation conditions [53]. Practically, a well passivated surface usually requires an additional layer, several nanometers in thickness, of the selected dielectrics. For simplicity, this additional passivation layer is neglected when modeling the passivated TPV configurations. In this paper, 10^4 cm/s and 10^2 cm/s are used to represent a non-passivated surface and a passivated surface, respectively. By comparing the BGR with the BSR under the same passivation condition, the effect of the external luminescence loss can be explicitly distinguished from that of surface passivation. The front

surfaces of four calculations are all assumed to be well-passivated. The surface recombination velocities for each TPV cell are listed in Table 1.

Table 1. Surface recombination velocities for each TPV cell

TPV cells	$S_{e,p}$ (cm/s)	$S_{h,p}$ (cm/s)	$S_{e,n}$ (cm/s)	$S_{h,n}$ (cm/s)
Passivated BSR/BGR	10^2	10^9	10^9	10^2
Non-passivated BSR/BGR	10^2	10^9	10^9	10^4

3.1. Output electric power and photogeneration rate

We first investigate a far-field TPV device with a 1 mm vacuum spacing. The effects of the back reflectors and surface passivation on the current density and voltage characteristic curves (i.e., the *J-V* curve) of this TPV cell are shown in Fig. 2a. The passivated TPV devices exhibit better *J-V* curves than those with a non-passivated condition. The generated current recombines at the non-passivated surface; a passivated TPV has a larger generated current than that of the non-passivated TPV. Under the same passivation conditions, the performance of TPV-BGR exceeds that of TPV-BSR. The working voltage of the passivated TPV-BGR is 0.062 V, which is 0.008 V larger than that of the passivated TPV-BSR. Hence, the passivated TPV-BGR can provide a maximum output power of 0.0061 W/cm^2, which is 38% larger than that of the passivated TPV-BSR. The performance enhancement can be explained by plotting the spectral photogeneration rates of these TPV devices shown in Fig. 2b. The spectral photogeneration rate of TPV-BGR is larger than that of TPV-BSR for both passivated and non-passivated condition. The enhanced spectrum of the photogeneration rates of TPV-BGR compared to that of TPV-BSR is 0.354 eV to 0.5 eV, because the external luminescence losses of TPV-BGR are greatly reduced. Moreover, the reflections at the semiconductor-vacuum interface of TPV-BGR is more efficient than those at the semiconductor-metal interface of TPV-BSR, since fewer photons above the bandgap energy are absorbed by the back metal. Note that the passivation condition has little effect on the photogeneration rate of TPV-BGR since external luminescence is minimized in this structure.

The maximum output power and photogeneration rate of four far-field TPV configurations as a function of the gap thickness are shown in Fig. 2c and 2d. As is clearly shown in Fig. 2c, the maximum output power of TPV-BGR slightly increases to a saturated value as the gap thickness increases. The enhancement effect on the output power of the TPV-BGR is demonstrated by

comparison with TPV-BSR. The maximum output power of TPV-BGR is 15%-40% higher, compared to TPV-BSR for the passivated condition. Although the maximum output power of the non-passivated condition is reduced by almost one third of the passivated condition, the maximum output power of TPV-BGR is 5%-15% larger than that of TPV-BSR for the non-passivated condition. Enhanced total net photogeneration rate and a well-passivated surface can greatly improve the maximum output power of a TPV device. Shown in Fig. 2d, the total net photogeneration rate of TPV-BGR exhibits a similar trend as Fig. 2c. As the total net photogeneration rate increases with the gap thickness, more free electrons and holes are generated in the TPV cell, which produces a larger output power than that of TPV-BSR. The total net photogeneration rate of TPV-BGR (passivated/non-passivated) is 10%-25% greater than that of the passivated TPV-BSR and 3%-15% larger than that of the non-passivated TPV-BSR. The enhancement effect on the total net generation rate of the passivated TPV-BGR is lower than that on the maximum output power, which is due to external luminescence at different photon chemical potentials. The total net photogeneration rate of InAs can be expressed by subtracting external luminescence from the net photogeneration rate between the emitter and the InAs. A good surface passivation would result in a larger photon chemical potential, which can result in a larger external luminescence. Although the total net photogeneration rate of the non-passivated TPV-BSR is larger than that of the passivated TPV-BSR, the generated free carriers in the non-passivated TPV-BSR recombine at the surfaces. Therefore, the passivated TPV-BSR has better performance than the non-passivated case. In summary, TPV-BGR with good passivated surfaces can definitely enhance the maximum output power at the far-field regime for different gap thicknesses.

The *J-V* curves and spectral photogeneration rates of a near-field TPV device with different back reflectors and passivation conditions are shown in Fig. 3a and 3b. Although the difficulty of fabricating a near-field TPV device with two 10 nm vacuum gaps is incredible, the back gap thickness of TPV-BGR is chosen to be 10 nm for numerical demonstration purposes. As shown in Fig. 3a, the open circuit voltages of the passivated TPVs are larger than that of the non-passivated TPVs. The surface recombination effects become more significant in the near-field case because a larger current density is generated and more free carriers recombine at the non-passivated surfaces. The working voltage of the passivated TPV-BGR is 0.143 V, which is 0.007 V larger than that of the passivated TPV-BSR. Hence, the passivated TPV-BGR exhibit a maximum output power of 0.63 W/cm^2, which 8% larger than that of the passivated TPV-BSR. Unlike the far-field

case, the enhancement of the *J-V* curve by replacing a BSR with a BGR is rather limited, because the photogeneration rate is dominated by the near-field radiation, which is not sensitive to the structure of the back reflectors. As shown in Fig. 3a, a well-passivated surface can greatly improve the maximum output power by increasing the open-circuit voltage for both the TPV-BGR and TPV-BSR. As shown in Fig. 3c, the maximum output power of the TPV-BGR decreases as the gap thickness increases for both passivated and non-passivated conditions. Whether TPV-BGR can provide enhancement on the maximum output power compared to TPV-BSR depends on the gap thickness. The largest enhancement provided by TPV-BGR is when the gap thickness equals 10 nm. The maximum output power generated by TPV-BGR has an 8% enhancement compared to that of the passivated TPV-BSR. In addition, the maximum improvement of TPV-BGR is reduced to 2.5% for the non-passivated condition. The surface passivation effect on the maximum output power is more dominant than the effect brought by the back reflector structure. The trend of the maximum output power of TPV-BGR matches well with the total net photogeneration rate, shown in Fig. 3d. Unlike the far-field condition, the reduction of the total net photogeneration rate as the gap thickness increases is not only due to the propagating photons but also the frustrated photons, which is represented by the difference between BGR and BGR Prop in Fig. 3d. As the gap thickness increases, the destructive absorption pattern causes a slight decrease in the total net photogeneration for the near-field condition. To summarize the effect of the gap thickness for the near-field condition, a BGR with a small gap thickness (comparable to vacuum spacing) is preferred for larger output power.

3.2. Efficiency and cell absorbed power

The improvement of maximum conversion efficiency brought by the BGR structure is clearly shown in Fig. 4. TPV-BGR exhibits improvement to the maximum conversion efficiency of TPV devices. As seen in Fig. 4a, the conversion efficiency using a BGR is 1.05-1.34 times higher than that using a BSR for non-passivated condition. The passivated TPV-BGR maximum efficiency ranges between 5.7%-7.4%, which is a 1.18-1.62 times higher than that of the passivated TPV-BSR when the gap thickness increases. This enhancement in efficiency is higher than that of the output power (15%-40%) indicating that the efficiency improvement is a coupled effect of the output power enhancement and parasitic absorption reduction. As clearly shown in Fig. 4b, the cell absorbed power is inversely correlated with the maximum efficiency as the gap thickness

increases. The reduction effect on cell absorbed power can be clearly seen by the difference between BGR and BSR. The cell absorbed power is dominated by the emission from the emitter, where the temperature is fixed at 900 K. The external luminescence from the InAs to vacuum at the back is negligible. Therefore, the passivated conditions have little effect on the cell absorbed power for both TPV-BSR and TPV-BGR. The same conclusion can be drawn for the near-field condition.

For the near-field condition shown in Fig. 5a, the passivated TPV-BGR has an 18%-21% maximum conversion efficiency when the gap thickness increases, which is higher than the 16.4% for the passivated TPV-BSR. For the non-passivated scenario, TPV-BGR also possesses a 1.08-1.19 times improvement when compared with TPV-BSR. As manifest in Fig. 5a, the maximum efficiency of TPV-BGR increases by increasing the gap thickness. Since the maximum output power of TPV-BGR is not a strong function of the gap thickness, the cell absorbed power of TPV-BGR should be inversely proportional to gap thickness to match the efficiency enhancement, which is exactly the trend of TPV-BGR shown in Fig. 5b. Compared to the propagating modes represented by the dashed-diamond curve, the cell absorbed power of TPV-BGR carried by the frustrated modes (the difference between the BGR and BGR Prop) is largely reduced in the near-field scenario. Near-field radiation dominates the radiation exchange between the emitter and cell, as the vacuum spacing decreases from Fig. 4b (d = 1 mm) to Fig. 5b (d = 10 nm). The efficiency enhancement brought by the BGR structure is apparently large.

3.3. Imperfect reflections and external luminescence loss of the back reflectors

The generated power can be enhanced by adding a conventional metal BSR to a TPV cell [37, 41, 42]. An ideal back reflector reflects all incident photons. However, a perfect mirror for photons of all wavelengths does not exist. The absorption of the back reflector occupies a significant amount of the parasitic absorption, which requires extra cooling power to maintain the TPV cells at a comfortable temperature range. Therefore, it is important to minimize the parasitic absorption of TPV cells. When light transmits through the semiconductor-metal interface of a TPV-BSR, the reflection is not perfect because most of the electromagnetic waves can easily transmit from an optically rare medium to an optically dense medium. However, by adding a gap between the semiconductor and the back reflector, most of the propagating photons reflect perfectly at the semiconductor-air interface through total internal reflection. However, if the gap thickness is

comparable to or less than the wavelength of transmitted photons, the photon tunneling effect would also be present between the semiconductor and the back metal. Therefore, the gap thickness is required to be larger than the characteristic wavelength to avoid photon tunneling effects and to minimize the absorption of the back reflector. In Fig. 6a and 6b, it is shown that the absorption in the BGR decreases significantly as the gap thickness increases for both far- and near-field regimes. When one compares the absorbed power of the metal in Fig. 6a with the cell absorbed power in Fig. 4b for TPV-BGR, the percentage of the absorbed power of the metal over the cell absorbed power is reduced from 38% to 14% when the gap thickness is increased from 10 nm to 1 μm. Hence, increasing the gap thickness of the BGR structure can greatly reduce the metal absorption to improve the performance of a far-field TPV device. As the gap thickness increases from 10 nm to 1 μm (or larger) in the near-field TPV-BGR in Fig. 6b, the percentage of the absorbed power of the metal over the cell absorbed power is reduced from 17% to 1% and the absorbed power carried by the frustrated modes are almost reduced to zero. This indicates that a TPV-BGR with a larger back gap can effectively reduce the absorption of the metal. Note that thermal radiation from the emitter and external luminescence from the InAs both contribute to the absorption of the back metal. The absorption of the metal in the BGR structure is not affected by the passivation condition because the incoming thermal radiation is dominating the absorption of the metal and external luminescence has been minimized with the TPV-BGR. However, the surface passivation conditions do affect the operating voltages of TPV-BSRs as shown in Fig. 2a and 2b, and external luminescence is exponentially related with the photon chemical potential, which is equal to the operating voltage times the elementary charge at low-level injection condition [44]. Therefore, the metal absorbs more power due to a higher external luminescence in the passivated TPV-BSR than the non-passivated case. This is shown for both far- and near-field condition in Fig. 6a and 6b, respectively.

The spectral absorbed powers of the metal in different TPV configurations provides more information about the reduction of the parasitic absorption, which are shown in Fig. 7a and 7b. For both far-and near-field TPV devices, two key comparisons should be carefully considered: TPV-BSR versus TPV-BGR and passivated TPV-BSR versus non-passivated TPV-BSR. For the far-field condition shown in Fig. 7a, the spectral absorbed power of the metal in the non-passivated TPV-BGR is lower than that in the non-passivated TPV-BSR, because the photon tunneling from the InAs region to the metal is suppressed for photons of all wavelengths. The spectral absorbed

power of the metal in the non-passivated TPV-BSR overlaps with the passivated TPV-BSR below the bandgap energy, since the absorption of the sub-bandgap photons is not related with surface passivation but the TPV structures. The external luminescence loss happens at the spectrum above the bandgap. The passivated TPV-BSR has greater external luminescence losses than the non-passivated case due to larger operating voltage. Therefore, the spectral absorbed power in the metal is larger for the photons above bandgap energy. The same conclusion can be drawn for the near-field condition shown in Fig. 7b. For both far- and near-field, the TPV-BGR can greatly reduce the absorption of the back reflectors, which is the key mechanism to improve the efficiency of a TPV device.

In a working TPV cell, the more electron and hole pairs are generated, the more likely they will recombine and generate external luminescence, similar to a biased LED [43, 44, 57]. The energies of luminescent photons are larger than bandgap. It is illustrated that the external luminescence intensity from a working TPV cell is exponentially proportional to the photon chemical potential, which is usually assumed to be equal to the product of the working voltage and elementary charge. The luminescent photons from the cell cannot be recycled when they are absorbed by any object other than the emitter and cell; this is called external luminescence loss. As one of the major loss mechanisms that deteriorates the performance of TPV devices working at moderate temperatures, the external luminescence loss can also be minimized by the BGR structure. As shown in Fig. 8a, at the maximum output power voltage (V_{max}), the passivated TPV-BGR at V_{max} = 0.054 V would emit ~10% photons of the total net photogeneration rate at the same condition. The external luminescent photon rate over the total net photogeneration rate is called external luminescence loss ratio. Due to the dominant effects of surface recombination in the non-passivated TPV-BSR, V_{max} is only 0.022 V, which is much less than that of the passivated TPV-BSR. Nevertheless, a 2% external luminescence loss ratio still exists in the non-passivated TPV-BSR. However, the external luminescence loss can be reduced to 1% of the total net photogeneration rate by introducing a 10 nm gap between the semiconductor and the back reflector. As the gap thickness increases, the external luminescence loss ratio can be reduced to less than 0.01%. Similar trends are exhibited in Fig 8b. The external luminescence loss ratio can be effectively reduced to zero by the BGR structure for both the passivated and non-passivated condition. Although V_{max} increases when the vacuum spacing reduces, the BGR structure can still reduce the external luminescence losses to negligible levels. Moreover, when the emitter

temperature increases, the TPV devices will be working at a higher voltage, which means a larger external luminescence would occur. Therefore, minimizing the external luminescence loss become even more critical at high emitter temperatures and the BGR structure is definitely useful in creating a high-performance TPV device.

3.4. Effect of the vacuum spacing on the maximum output power and maximum efficiency

To study the effect of the vacuum spacing on the TPV with different back reflectors, a parametric analysis on the vacuum spacing is performed for the four TPV devices. To clearly show the effect of the BGR structure on the performance of TPV devices, the back gap thickness is fixed at 1 μm, which is feasible for current fabrication technologies. In general, the maximum output powers and maximum efficiency of all TPV devices decrease as the vacuum spacing increases shown in Fig. 9a and 9b. The passivated cases exhibit better maximum output powers than the non-passivated cases. The maximum output power of TPV devices can be improved by replacing the BSR with the BGR (h = 1 μm) when the vacuum spacing is larger than hundreds of nanometers. When the vacuum spacing is in the near-field regime (d < 100 nm), TPV-BGR does not provide higher output powers when compared with the TPV-BSR. However, the maximum efficiency of TPV devices can benefit from the BGR structure for both far- and near-field regimes. In summary, the BGR structure can improve the performance of the far-field TPV devices; while in the near-field condition, the back gap thickness should be carefully chosen to simultaneously increase the maximum output power and efficiency of TPV devices.

4. **Conclusions**

This work theoretically demonstrates the performance improvement of a thin-film InAs TPV device by replacing the conventional metal BSR with a BGR. A coupled photon-charge transport model that accounts for surface recombination and external luminescence is used to model these two TPV devices for both far- and near-field regimes. The performance improvement due to this BGR structure is addressed when compared with the TPV-BSR. The results show that the output power and efficiency are significantly improved for far-field TPV-BGR. Moreover, the near-field InAs TPV devices with a BGR also exhibit a ~10% improvement of the output power and an efficiency boost of 4.5% (absolute value) over BSR under well-passivation condition. The performance enhancement brought by the well-passivated back surface is huge for both BSR and BGR. The absorption of the metal is significantly reduced by adding a gap between the

semiconductor and back reflector for both far- and near-field TPV devices. The external luminescence loss is significantly reduced in TPV-BGR. The parametric sweeps on the gap thickness of BGR and the vacuum spacing provide a clear direction for the design and optimization for both far- and near-field TPV devices.

Acknowledgement

This work was supported by the U.S. Department of Energy, Office of Science, Basic Energy Sciences (DE-SC0018369).

Data availability

The data that support the findings of this study are available from the corresponding authors upon reasonable request.

References

[1] S. Akhtar, J. C. Kurnia, and T. Shamim, A three-dimensional computational model of H_2–air premixed combustion in non-circular micro-channels for a thermo-photovoltaic (TPV) application, Appl. Energy 152 (2015) 47-57.

[2] K. F. Mustafa, S. Abdullah, M. Z. Abdullah, and K. Sopian, A review of combustion-driven thermoelectric (TE) and thermophotovoltaic (TPV) power systems, Renewable Sustainable Energy Rev. 71 (2017) 572-584.

[3] Q. Lu, X. Zhou, A. Krysa, A. Marshall, P. Carrington, C. H. Tan, and A. Krier., InAs thermophotovoltaic cells with high quantum efficiency for waste heat recovery applications below 1000°C, Sol. Energy Mater. Sol. Cells 179 (2018) 334-338.

[4] T. J. Coutts, An overview of thermophotovoltaic generation of electricity, Sol. Energy Mater. Sol. Cells 66 (2001) 443-452.

[5] A. Datas and A. Martí, Thermophotovoltaic energy in space applications: Review and future potential, Sol. Energy Mater. Sol. Cells 161 (2017) 285-296.

[6] V. L. Teofilo, P. Choong, J. Chang, Y. L. Tseng, and S. Ermer, Thermophotovoltaic energy conversion for space, J. Phys. Chem. C 112 (2008) 7841-7845.

[7] B. Wernsman, R. G. Mahorter, R. Siergiej, S. D. Link, R. J. Wehrer, S. J. Belanger, P. Fourspring, S. Murray, F. Newman, D. Taylor, and T. Rahmlow, Advanced thermophotovoltaic devices for space nuclear power systems, AIP Conf. Proc. 746 (2005) 1441-1448.

[8] T. M. Regan, J. G. Martín, and J. Riccobono, TPV conversion of nuclear energy for space applications, AIP Conf. Proc. 321 (1995) 322-330.

[9] Z. Zhou, E. Sakr, Y. Sun, and P. Bermel, Solar thermophotovoltaics: reshaping the solar spectrum, Nanophoton. 5 (2016) 1-21.

[10] A. Lenert, D. M. Bierman, Y. Nam, W. R. Chan, I. Celanović, M. Soljačić, E. N. Wang, A nanophotonic solar thermophotovoltaic device, Nat. Nanotechnol. 9 (2014) 126-130.

[11] A. Datas, D. L. Chubb, and A. Veeraragavan, Steady state analysis of a storage integrated solar thermophotovoltaic (SISTPV) system, Sol. Energy 96 (2013) 33-45.

[12] Y. Wang, H. Liu, and J. Zhu, Solar thermophotovoltaics: Progress, challenges, and opportunities, APL Mater. 7 (2019) 080906.

[13] Z. Omair, G. Scranton, L. M. Pazos-Outón, T. P. Xiao, M. A. Steiner, V. Ganapati, P. F. Peterson, J. Holzrichter, H. Atwater, E. Yablonovitch, Ultraefficient thermophotovoltaic power conversion by band-edge spectral filtering, Proc. Natl. Acad. Sci. 116 (2019) 15356-15361.

[14] A. Datas, C. Algora, J. C. Zamorano, V. Corregidor, D. Martin, A. W. Bett, F. Dimroth, J. Fernandez, M. Baudrit, and B. Hernandez, A solar TPV system based on germanium cells, AIP Conf. Proc. 890 (2007) 280-290.

[15] D. M. Bierman, A. Lenert, W. R. Chan, B. Bhatia, I. Celanović, M. Soljačić, and E. N. Wang, Enhanced photovoltaic energy conversion using thermally based spectral shaping, Nat. Energy 1 (2016) 16068.[16] A. Datas and C. Algora, Development and experimental evaluation of a complete solar thermophotovoltaic system, Prog. Photovoltaics Res. Appl. 21 (2013) 1025-1039.

[17] N.-P. Harder and P. Wurfel, Theoretical limits of thermophotovoltaic solar energy conversion, Semicond. Sci. Tech. 18 (2003) S151-S157.

[18] R. Bhatt, I. Kravchenko, and M. Gupta, High-efficiency solar thermophotovoltaic system using a nanostructure-based selective emitter. Sol. Energy 197 (2020) 538-545.

[19] S. Basu, Y.-B. Chen, and Z. M. Zhang, Microscale radiation in thermophotovoltaic devices—A review, Int. J. Energy Res. 31 (2007) 689-716. [20] T. Bauer, Thermophotovoltaics: Basic Principles and Critical Aspects of System Design, Springer, Berlin, 2011.

[21] Y. B. Chen and Z. M. Zhang, Design of tungsten complex gratings for thermophotovoltaic radiators, Opt. Commun. 269 (2007) 411-417.

[22] B. Zhao, L. Wang, Y. Shuai, and Z. M. Zhang, Thermophotovoltaic emitters based on a two-dimensional grating/thin-film nanostructure, Int. J. Heat Mass Transfer 67 (2013) 637-645.

[23] H. Sai, Y. Kanamori, and H. Yugami, Tuning of the thermal radiation spectrum in the near-infrared region by metallic surface microstructures, J. Micromech. Microeng. 15 (2005) S243-S249.

[24] L. P. Wang and Z. M. Zhang, Wavelength-selective and diffuse emitter enhanced by magnetic polaritons for thermophotovoltaics, Appl. Phys. Lett. 100 (2012) 063902.

[25] V. Tomer, R. Teye-Mensah, J. C. Tokash, N. Stojilovic, W. Kataphinan, E. A. Evans, G. G. Chase, R. D. Ramsier, D. J. Smith, and D. H. Reneker, Selective emitters for thermophotovoltaics: erbia-modified electrospun titania nanofibers, Sol. Energy Mater. Sol. Cells 85 (2005) 477-488.

[26] A. Narayanaswamy and G. Chen, Thermal emission control with one-dimensional metallodielectric photonic crystals, Phys. Rev. B 70 (2004) 125101.

[27] D. Cakiroglu, J. P. Perez, A. Evirgen, C. Lucchesi, P. O. Chapuis, T. Taliercio, E. Tournié, and R. Vaillon, Indium antimonide photovoltaic cells for near-field thermophotovoltaics, Sol. Energy Mater. Sol. Cells 203 (2019) 110190.

[28] M. D. Whale and E. G. Cravalho, Modeling and performance of microscale thermophotovoltaic energy conversion devices, IEEE Trans. Energy Conv. 17 (2002) 130-142.

[29] Z. M. Zhang, Nano/Microscale Heat Transfer, 2nd ed., Springer Nature, Cham, 2020.

[30] M. Ghashami, A. Jarzembski, M. Lim, B. J. Lee, and K. Park, Experimental exploration of near-field radiative heat transfer, Ann. Rev. Heat Transfer 23 (2020) 13-56.

[31] G. R. Bhatt, B. Zhao, S. Roberts, I. Datta, A. Mohanty, T. Lin, J. M. Hartmann, R. St-Gelais, S. Fan, and M. Lipson, Integrated near-field thermo-photovoltaics for heat recycling, Nat. Commun. 11 (2020) 2545.

[32] A. Fiorino, L. Zhu, D. Thompson, R. Mittapally, P. Reddy, and E. Meyhofer, Nanogap near-field thermophotovoltaics, Nat. Nanotechnol. 13 (2018) 806-811.

[33] T. Inoue, T. Koyama, D. D. Kang, K. Ikeda, T. Asano, and S. Noda, One-chip near-field thermophotovoltaic device integrating a thin-film thermal emitter and photovoltaic cell, Nano Lett. 19 (2019) 3948-3952.

[34] C. Lucchesi, D. Cakiroglu, J.P. Perez, t. Taliercio, E. Tournié, P.O. Chapuis, and R. Vaillon, Near-Field Thermophotovoltaic Conversion with High Electrical Power Density and Cell Efficiency above 14%, Nano Lett. 21 (2021) 4524-4529.

[35] R. Mittapally, B. Lee, L. Zhu, A. Reihani, J.W. Lim, D. Fan, S.R. Forrest, P. Reddy, and E. Meyhofer, Near-field thermophotovoltaics for efficient heat to electricity conversion at high power density, Nat. Commun. 12 (2020) 1-8.

[36] J. I. Watjen, X. L. Liu, B. Zhao, and Z. M. Zhang, A computational simulation of using tungsten gratings in near-field thermophotovoltaic devices, J. Heat Transfer 139 (2017) 052704.

[37] K. Park, S. Basu, W. P. King, and Z. M. Zhang, Performance analysis of near-field thermophotovoltaic devices considering absorption distribution, J. Quant. Spectrosc. Radiat. Transfer 109 (2008) 305-316.

[38] B. Zhao, K. Chen, S. Buddhiraju, G. Bhatt, M. Lipson, and S. Fan, High-performance near-field thermophotovoltaics for waste heat recovery, Nano Energy 41 (2017) 344-350.

[39] O. Ilic, M. Jablan, J. D. Joannopoulos, I. Celanovic, and M. Soljačić, Overcoming the black body limit in plasmonic and graphene near-field thermophotovoltaic systems, Opt. Express 20 (2012) A366-A384.

[40] T. Burger, C. Sempere, B. Roy-Layinde, and A. Lenert, Present efficiencies and future opportunities in thermophotovoltaics, Joule 4 (2020) 1660-1680

[41] T. J. Bright, L. P. Wang, and Z. M. Zhang, Performance of Near-field thermophotovoltaic cells enhanced with a backside reflector, J. Heat Transfer 136 (2014) 062701.

[42] J. Fernández, F. Dimroth, E. Oliva, M. Hermle, and A. W. Bett, Back-surface optimization of germanium TPV cells, AIP Conf. Proc. 890 (2007) 190-197.

[43] D. Feng, E. J. Tervo, S. K. Yee, and Z. M. Zhang, Effect of Evanescent Waves on the Dark Current of Thermophotovoltaic Cells, Nanos. Micros. Thermophys. Eng. 24 (2020) 1-19.

[44] D. Feng, E. J. Tervo, D. Vasileska, S. K. Yee, A. Rohatgi, and Z. M. Zhang, Spatial profiles of photon chemical potential in near-field thermophotovoltaic cells, arXiv:2103.14740.

[45] D. Fan, T. Burger, S. McSherry, B. Lee, A. Lenert, and S. R. Forrest, Near-perfect photon utilization in an air-bridge thermophotovoltaic cell, Nature, 586 (2020) 237-241.

[46] T. Inoue, T. Suzuki, K. Ikeda, T. Asano, and S. Noda, Near-field thermophotovotaic devices with surrounding non-contact reflectors for efficient photon recycling, Opt. Express, 29 (7) 11133-11143.

[47] W. A. Callahan, D. Feng, Z. M. Zhang, E. S. Toberer, A. J. Ferguson, and E. J. Tervo, Coupled charge and radiation transport processes in thermophotovoltaic and thermoradiative cells, Phys. Rev. Appl. 15 (2021) 054035.

[48] C. Henkel and K. Joulain, Electromagnetic field correlations near a surface with a nonlocal optical response, Appl. Phys. B 84 (2006) 61-68.

[49] K. Joulain, Near-field heat transfer: A radiative interpretation of thermal conduction, J. Quant. Spectrosc. Radiat. Transfer 109 (2008) 294-304.

[50] M. Sotoodeh, A. H. Khalid, and A. A. Rezazadeh, Empirical low-field mobility model for III–V compounds applicable in device simulation codes, J. Appl. Phys. 87 (2000) 2890-2900.

[51] M. A. Ordal, R. J. Bell, R. W. Alexander, L. A. Newquist, and M. R. Querry, Optical properties of Al, Fe, Ti, Ta, W, and Mo at submillimeter wavelengths, Appl. Opt. 27 (1988) 1203-1209.

[52] E. D. Palik, Handbook of Optical Constants of Solids, Academic Press, San Diego, 1998.

[53] M. Levinshtein and S. Rumyantsev, Handbook Series on Semiconductor Parameters. Vol. 1, Si, Ge, C (Diamond), GaAs, GaP, GaSb, InAs, InP, InSb, World Scientific Publishing, Singapore, 1996.

[54] Y. Da and Y. Xuan, Role of surface recombination in affecting the efficiency of nanostructured thin-film solar cells, Opt. Express, 21 (2013) A1065-A1077.

[55] E. Blandre, P. O. Chapuis, and R. Vaillon, High-injection effects in near-field thermophotovoltaic devices, Sci. Rep. 7 (2017) 15860.

[56] J. A. Nelson, The Physics of Solar Cells, World Scientific Publishing, Singapore, 2003.

[57] U. Rau, Reciprocity relation between photovoltaic quantum efficiency and electroluminescent emission of solar cells, Phys. Rev. B 76 (2007) 085303.

Figure captions

Fig. 1. Schematic of an InAs TPV device with (a) a BGR and (b) a conventional BSR. Here, d is the vacuum spacing between the emitter and the cell, and h is the back gap thickness. The TPV cell includes the InAs and the back reflector.

Fig. 2. (a) Current density and voltage characteristic curve and (b) spectral photogeneration rate of TPV-BSR and TPV-BGR (h = 1 μm) with different passivation conditions when d = 1 mm. (c) Maximum output power and (d) total net photogeneration rate as a function of the gap thickness of a TPV cell with different back reflectors and passivation conditions when d = 1 mm. To be noted for Fig. 2 and Fig. 3, the spectral photogeneration rate and total net photogeneration rate are calculated at the maximum output power condition for each TPV device. The BGR curves in Fig. 2b, 2d, 3b and 3d represent both the passivated and non-passivated TPV-BGR.

Fig. 3. (a) Current density and voltage characteristic curve and (b) spectral photogeneration rate of the TPV-BSR and TPV-BGR (h = 10 nm) with different passivation conditions when d = 10 nm. (c) Maximum output power and (d) total net photogeneration rate as a function of the gap thickness of a TPV cell with different back reflectors and passivation conditions when d = 10 nm.

Fig. 4. (a) Maximum conversion efficiency and (b) cell absorbed power as a function of the gap thickness for TPV devices with different back reflectors and passivation conditions when d = 1 mm. The surface passivation has little effect on the cell absorbed power, therefore, the BGR and the BSR represent both the passivated and non-passivated conditions in Fig. 4b and 5b.

Fig. 5. (a) Maximum conversion efficiency and (b) cell absorbed power as a function of the gap thickness for TPV devices with different back reflectors and passivation conditions when d = 10 nm.

Fig. 6. The absorbed power of the back metal (Q_{metal}) as a function of the gap thickness for TPV devices with different back reflectors when (a) d = 1 mm and (b) d = 10 nm.

To be noted, the BGR and BGR Prop represent both passivated and non-passivated condition since the surface passivation condition has little effect on the absorbed power of the metal.

Fig. 7. (a) Spectral absorbed powers of the metal in the TPV-BGR (h = 1 μm) and TPV-BSR when d = 1 mm. (b) Spectral absorbed powers of the metal in the TPV-BGR (h = 10 nm) and TPV-BSR when d = 10 nm. The passivation condition has little effect on the spectral absorbed power of the TPV-BGR so that the BGR curves in both Fig. 7a and 7b represent the passivation and non-passivated conditions.

Fig. 8. External luminescence loss ratio as a function of the gap thickness for TPV devices with different back reflectors when (a) d = 1 mm and (b) d = 10 nm at the maximum output power voltage.

Fig. 9. (a) Maximum output power and (b) maximum efficiency as a function of the vacuum spacing of a TPV device with different back reflectors and passivation conditions. The gap thickness of the TPV-BGR is fixed at h = 1 μm.

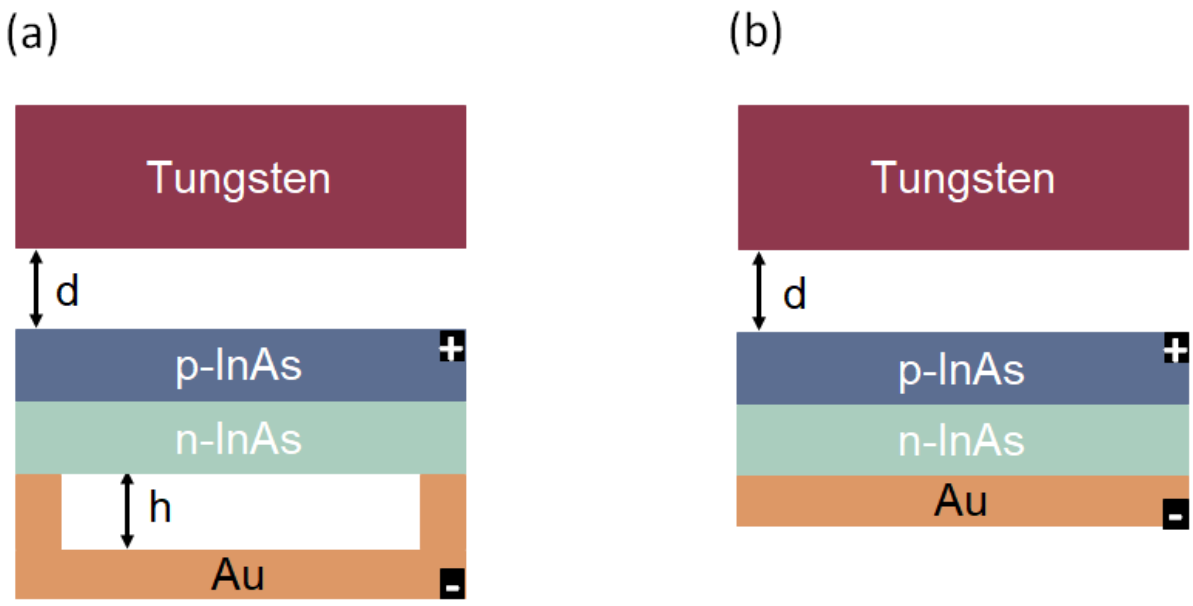

Fig. 1, Feng et al.

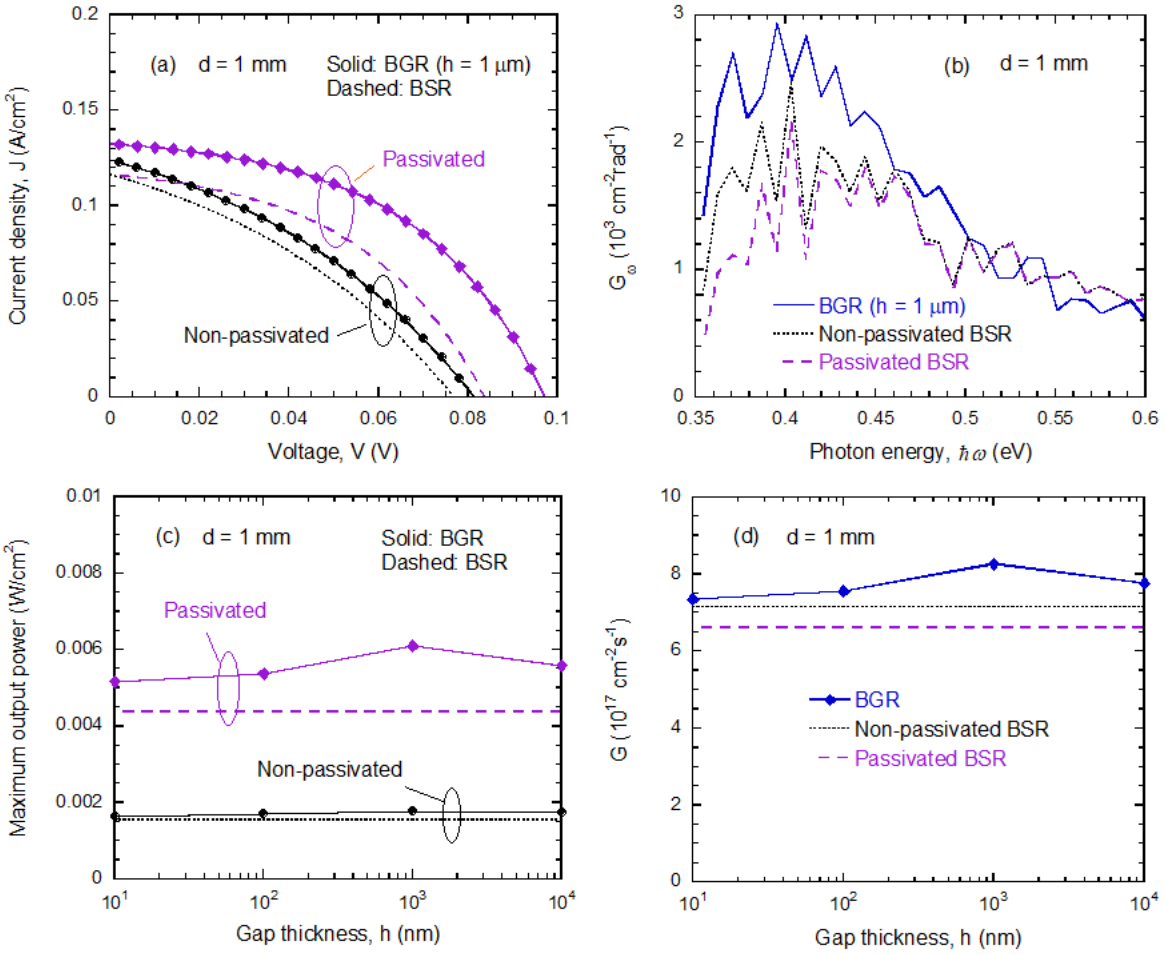

Fig. 2, Feng et al.

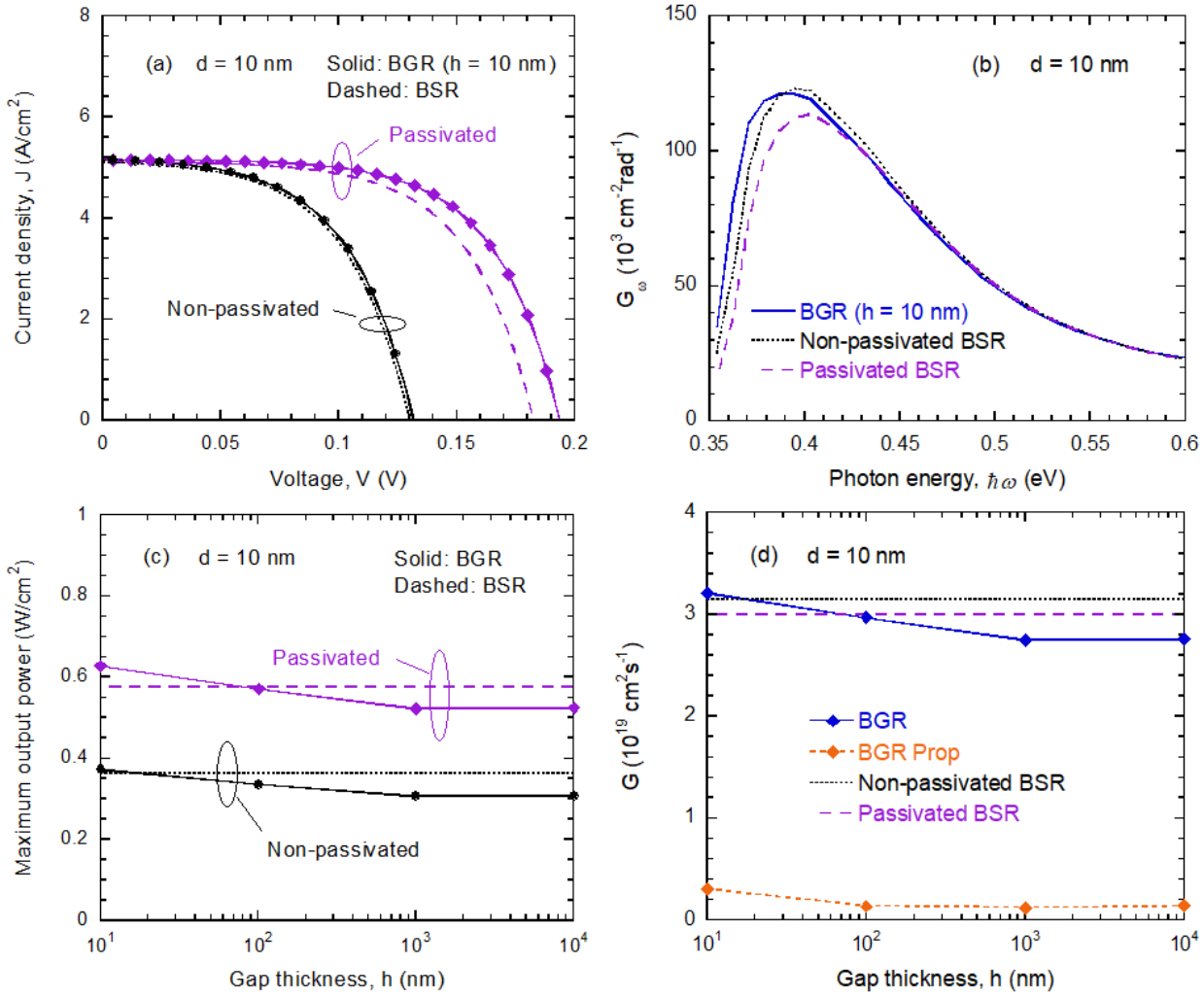

Fig. 3, Feng et al.

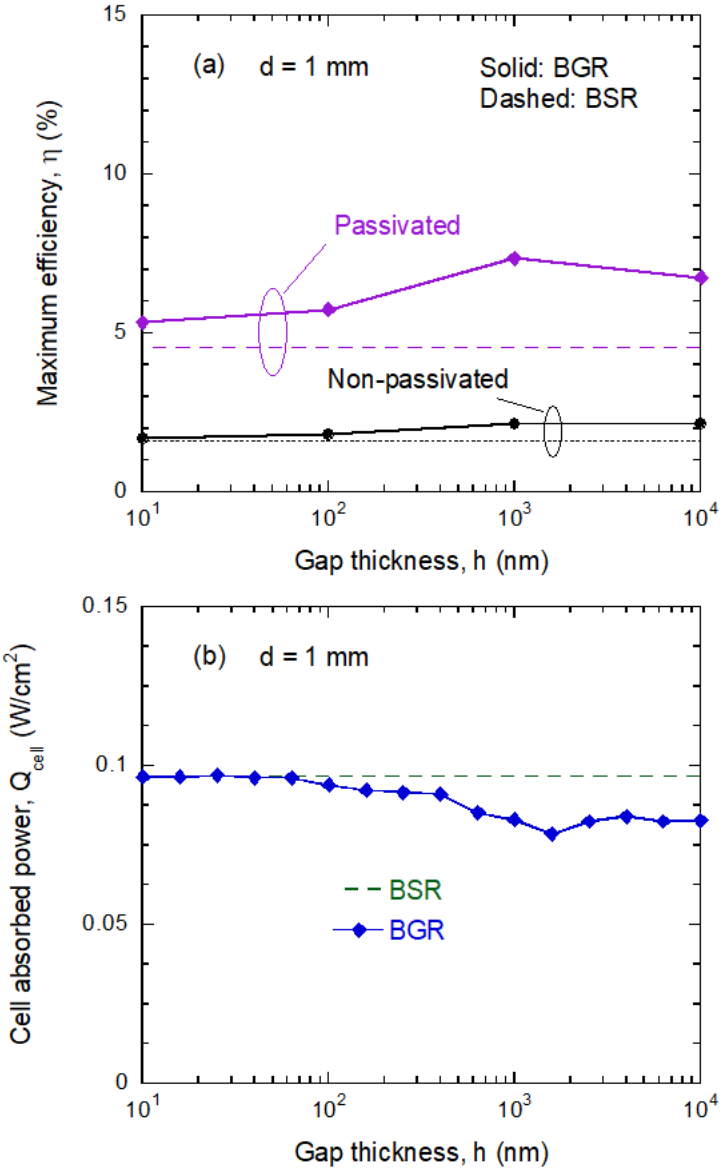

Fig. 4, Feng et al.

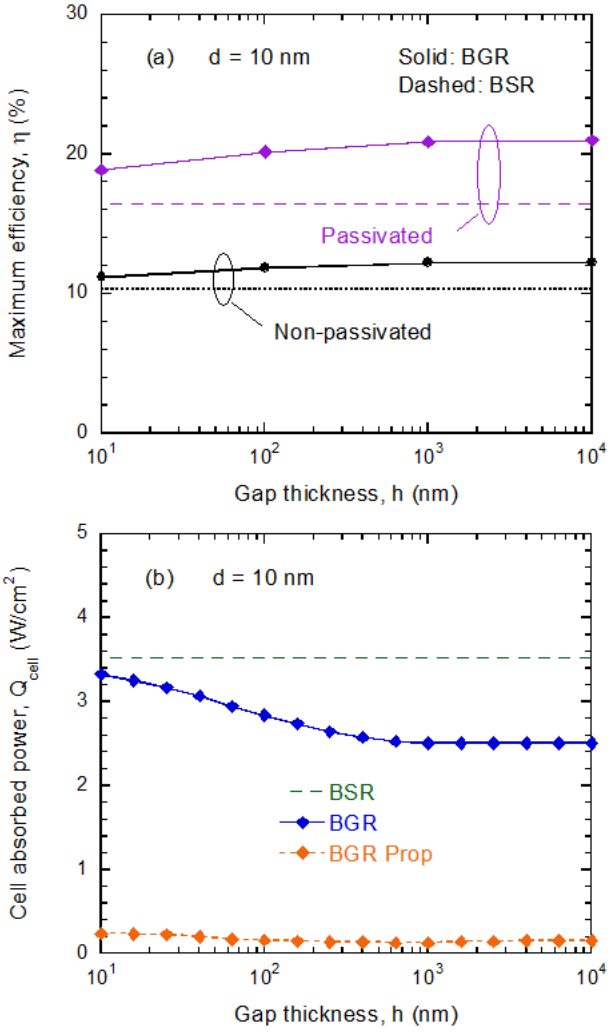

Fig. 5, Feng et al.

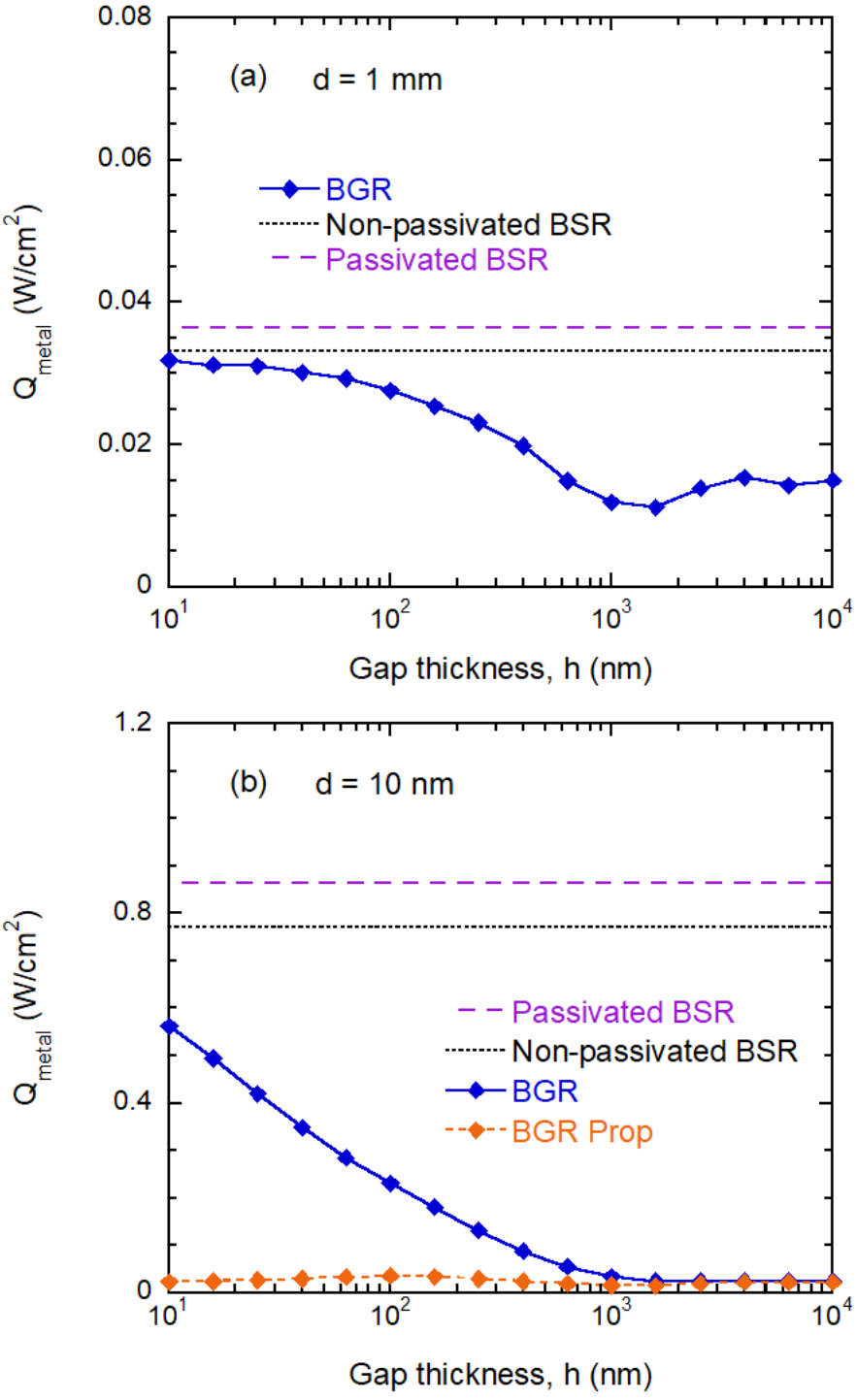

Fig. 6, Feng et al.

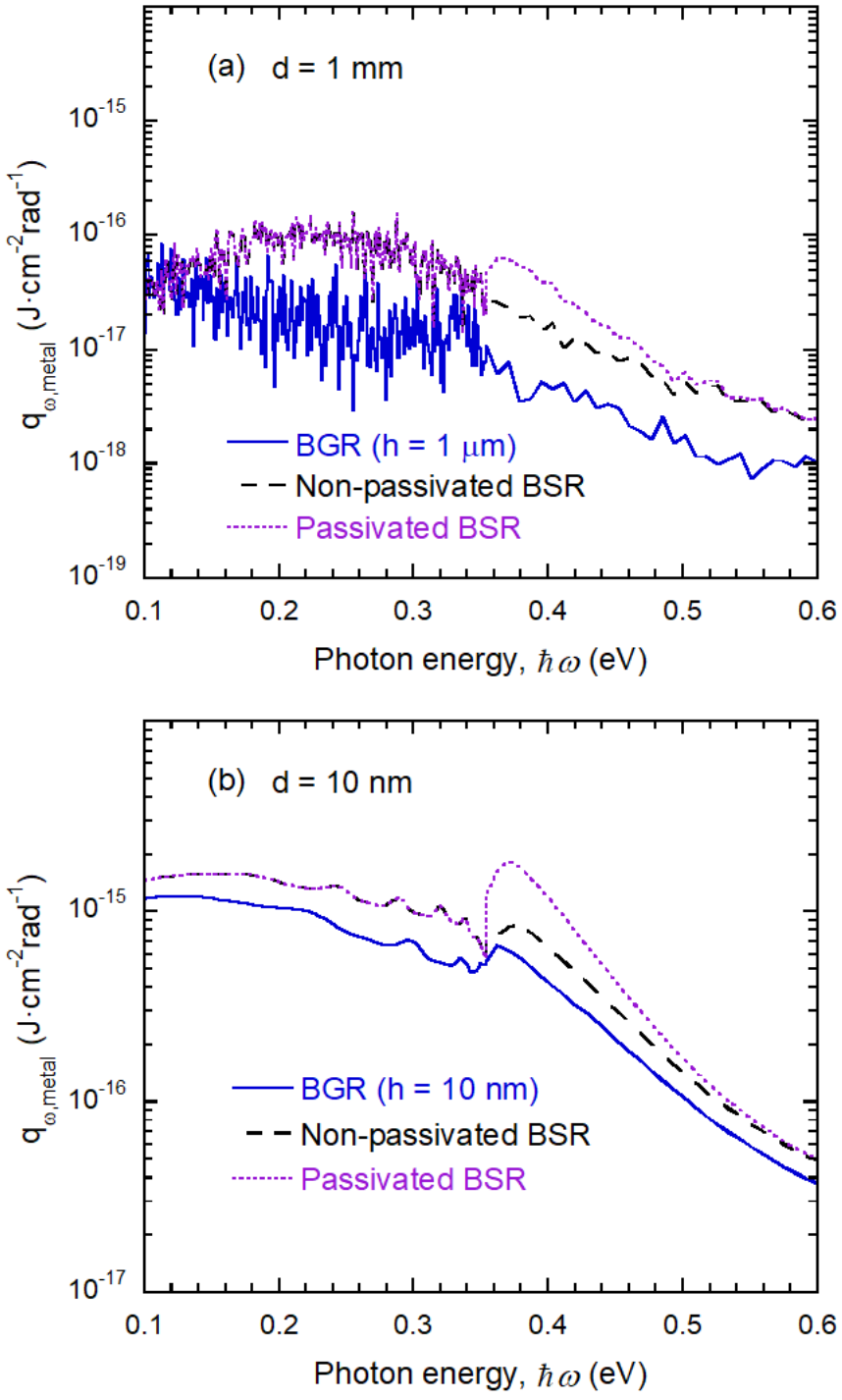

Fig. 7, Feng et al.

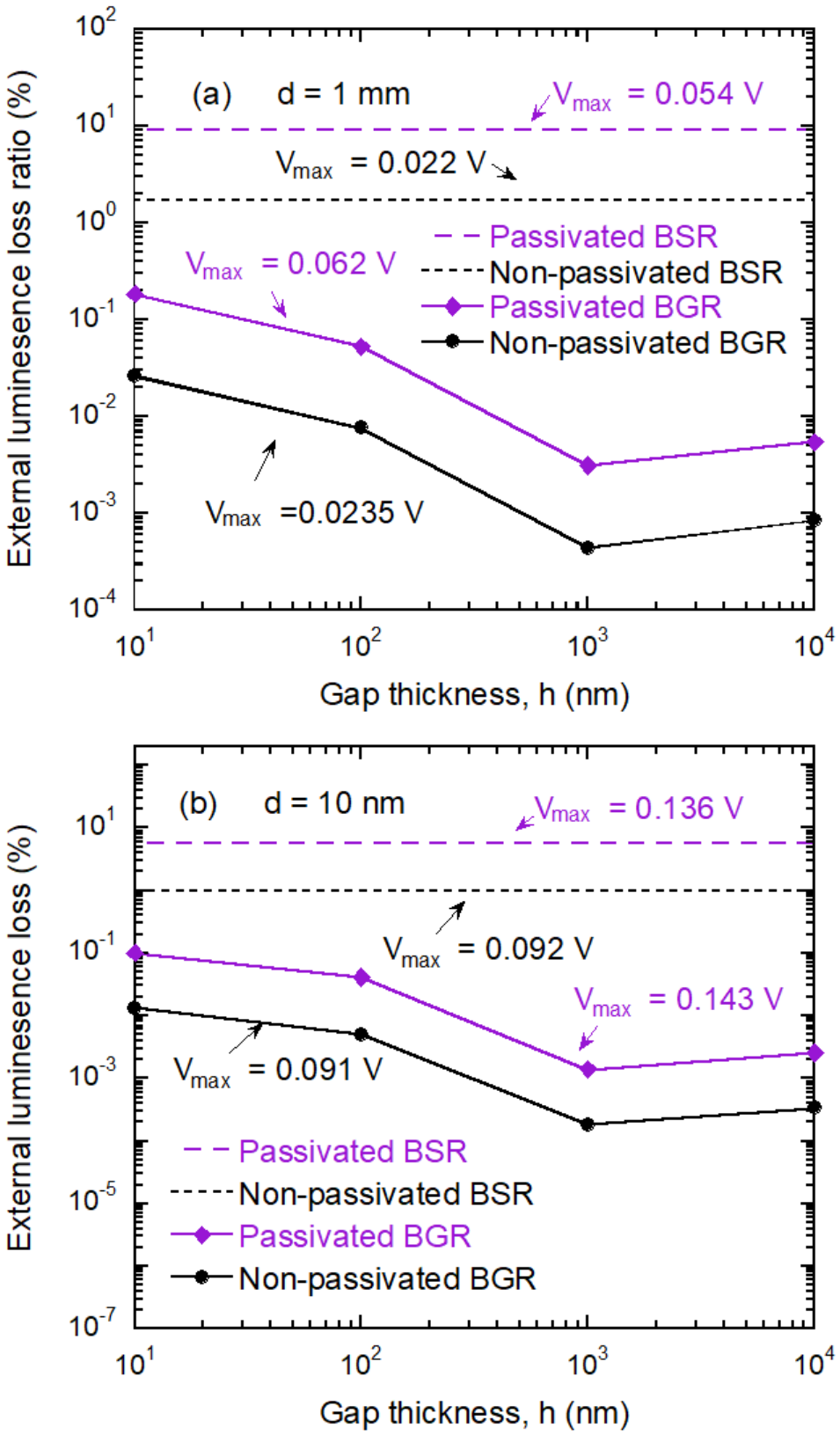

Fig. 8, Feng et al.

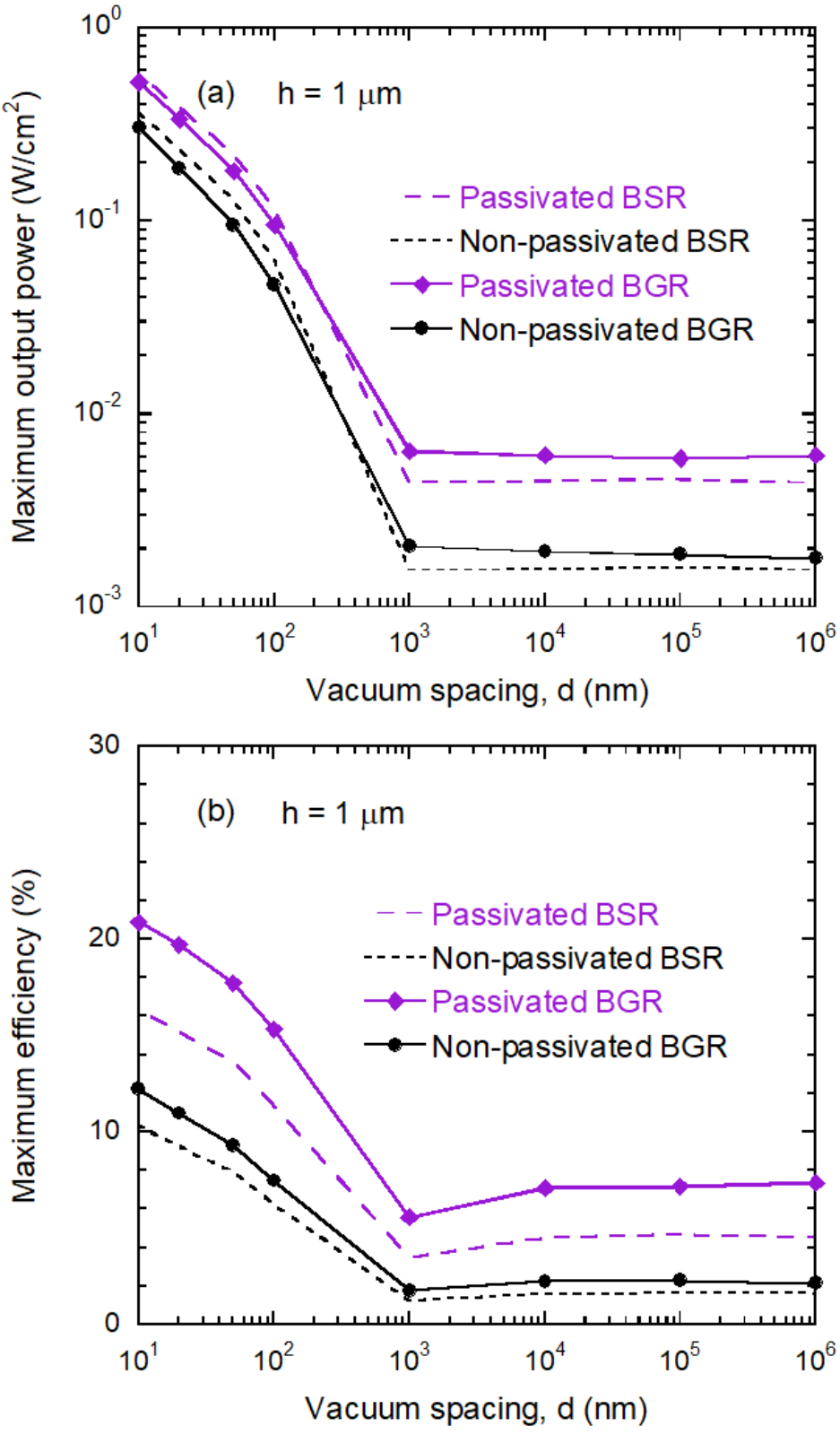

Fig. 9, Feng et al.